Available online at www.sciencedirect.com

ScienceDirect

Energy Procedia 00 (2015) 000–000

Energy Procedia

www.elsevier.com/locate/procedia

International Conference on Concentrating Solar Power and Chemical Energy Systems, SolarPACES 2014

Design and operation of an irradiance measurement network

H. Schenk[a], T. Hirsch[b], M. Wittmann[c], S. Wilbert[d], L. Keller[e], C. Prahl[f],

[a] *Researcher, M. Sc., German Aerospace Center (DLR), Institute of Solar Research, Wankelstraße 5, 70563 Stuttgart, Germany, Phone +49 711 6862 740, e-mail: Heiko.Schenk@dlr.de*

[b] *Team leader, Dr. -Ing, German Aerospace Center (DLR), Institute of Solar Research, Wankelstraße 5, 70563 Stuttgart, Germany, +49 711 6862 428.*

[c] *Researcher, Dr.-Ing., German Aerospace Center (DLR), Institute of Solar Research, Wankelstraße 5, 70563 Stuttgart, Germany, +49 711 6862 730. 4*

[d] *Researcher, Dipl.-Phys., DLR, Institute of Solar Research, Plataforma Solar de Almería, Ctra. De Senés s/n, km 4, 04200 Tabernas/Spain, +34 950 277619*

[e] *Researcher, Dipl.-Ing., DLR, Institute of Solar Research, Plataforma Solar de Almería, Ctra. De Senés s/n, km 4, 04200 Tabernas/Spain, +34 950 362 943*

[f] *Researcher, Dipl.-Phys., DLR, Institute of Solar Research, Plataforma Solar de Almería, Ctra. De Senés s/n, km 4, 04200 Tabernas/Spain, +34 950 265 883*

Abstract

The area covered by large-scale solar thermal power plants extends out to one up to several square kilometers. During the passage of clouds, the solar fields of these plants get partially shaded while other areas remain irradiated. In the case of line-focus plants these transient effects lead to inhomogeneous outlet temperatures of collector loops, while in point-focus plants the flux density at the receiver is influenced. Nowadays, yield prognoses based on measured irradiation data at one specific site, neglecting the effect of inhomogeneous irradiation. One of the aims of the Turikon project is to provide temporally and spatially resolved maps of direct normal irradiance (DNI). On this account, a distributed irradiance measurement network has been installed at the Plataforma Solar in Spain within the research activities of the Turikon project. The network, which consists of 20 silicon pyranometers and a data acquisition system, is in operation since 2013, delivering distributed values for the global horizontal irradiation with a temporal resolution of one Hertz. In the present work a methodology is presented, that makes use of measurements from the network and additionally a vector of cloud movement, derived from shadow pictures. In that manner, data points can be shifted in the direction of cloud movement in order to obtain a temporally resolved DNI map that overlaps the circumference of the measurement network. In this publication, an example is presented that already shows the good applicability of the methodology. Subsequently, the methodology will be tested and validated with a broader data-base.

Peer review by the scientific conference committee of SolarPACES 2014 under responsibility of PSE AG.

Keywords: distributed irradiation measurement; temporally resolved DNI-Maps; transient solar field operation

Peer review by the scientific conference committee of SolarPACES 2014 under responsibility of PSE AG.

1. Introduction

Large scale concentrated solar thermal electric plants may cover areas of one square kilometer and more. This large spatial extension implies that parts of the solar field are irradiated while other parts are shaded when clouds pass by. Systems based on line focusing concentrators usually react to such situations with loop outlet temperature deviations from the set points while point focusing concentrators like solar towers suffer from fast changes in flux density on the receiver. Compared to steady-state blue sky conditions varying irradiance on the field leads to reduced plant efficiency due to temperature drop or required defocusing of collectors, increase in parasitic consumption due to intensified control actions, and fortified life-time consumption of the components due to stress. The control system of the plant is designed for a maximum output while assuring safe operation. Since data on spatial distribution of irradiance disturbances have been sparse in the past, most of todays' plants in operation make use of rather conservative control schemes taking into account penalties in terms of efficiency. Having passed their acceptance tests and enforced by the modified legislation in Spain, plant operators start to optimize the control procedures of their plants. One of the issues to be analyzed is the improved reaction of the field to cloud passage.

In parallel to these pragmatic approaches of the plant operators, the scientific community aims at improving the knowledge on the spatial variations in irradiance and improved control strategies. A number of studies illustrate the effect of identical irradiance disturbances imposed on different locations along a collector loop. Examples for parabolic trough oil systems can be found in [1] or [2]. The impact becomes very clear especially for direct steam generation line focusing systems where the loop outlet temperatures strongly depend on the location of the shading [3]. Advances in control concepts for all types of concentrating thermal power plants can be reached with two prerequisites: 1) A simulation tool capable of representing large solar systems, either line focusing or tower systems and 2) the knowledge of appropriate irradiance boundary conditions as test setups for control design. The determination of appropriate irradiance data in high temporal and spatial resolution requires intense measuring activities which are currently in an early stage.

In principle, researchers follow two approaches for deriving maps of direct normal irradiance (DNI-maps). The first one is to use one or multiple sky imagers to identify clouds and calculate back their shadows on the ground. This technology is currently under development from various research teams world-wide eg. see [4]. Main challenges include the determination of cloud height and three-dimensional form as well as the effective opacity of the cloud. Apart from recording DNI-maps as test setups this technology offers the potential of delivering DNI map forecasts within a time horizon of up to 30 min. Such information could be used to improve control concepts by means of model predictive control systems. A second, more pragmatic, approach makes use of a high number of irradiance measurement devices installed on the ground. The challenge here lies in the installation, maintenance, and data acquisition of the signals. While a forecasting functionality is only given inside the area covered by the measurement grid, the sensors deliver irradiance information with rather low uncertainty (< 5 %).

Irradiance measurement networks for the analysis of spatially inhomogeneous radiance have been used in other studies (e.g. NREL's experiment in Oahu, Hawaii, [5] and the validation grid used by Chow et al. [6]. However, these networks are basically focused on the GHI and not on DNI. For interpolation between the grid points of a measurement network the vector of cloud motion has to be determined. Different methods have been reported in literature [7, 8]. This paper presents a new measurement grid installed at the solar test facility *Plataforma Solar de Almería* (PSA) in southern Spain. The grid consists of four measurement diamonds each equipped with five pyranometers. In addition, two cameras are installed at the top of a test facility tower at 85 m height to monitor shadows passing over the area. The initial purpose of the installation was to derive data sets of spatially resolved DNI in high temporal resolution as input boundary conditions for simulation studies. In the framework of the European Research project DNICast the data from the measurement grid will be used to validate new approaches based on sky images. The paper describes the setup of the measurement grid, operational experiences, and first DNI-maps.

2. Choice of sensors

In order to generate a spatially resolved irradiance map for an area given by a parabolic trough loop or the complete solar field, a high number of irradiance sensors is desirable. Pyrheliometers with solar trackers would entail high costs. Since several measurement stations at PSA already provide DNI and DHI measurements, the measurement network was built from unshaded pyranometers. By using the DHI from the existing measurement stations the pyranometers GHI signals can be transformed to an approximation for the DNI at the location of each pyranometer. The selection of the best sensors for a given budget does therefore depend on both, their accuracy and their costs, including the data acquisition. Various relatively inexpensive semiconductor pyranometers were considered. Besides three Si-pyranometers (Campbell CS 300 (named *CS* in plots), Kipp&Zonen SP-Lite 2 (*SP*), LI-COR Li-200 (*LI*); three sensors each) also 10 MSR 145 sensors of the Swiss company MSR were tested. The MSR 145 includes a lux-meter OSRAM SFH 5712, a battery-powered logger and an USB connection in a small plastic housing (1 x 1 x 6 cm³). During an extended measuring campaign, the four different sensors were compared with closely located thermopile pyranometer (Kipp&Zonen CMP11) and a Pyrheliometer (Kipp&Zonen CH1) with respect to derived DNI results. Both sensors are installed at the PSA-HP Meteostation (37.09 °N, -2.35 °E). Since the MSR 145 measure the illuminance, the relation between the measured illuminance and the GHI was investigated. The results of the MSR differ significantly. On the one hand, some MSR showed promising results, see Fig. 1. On the other hand, a strong nonlinearity between the two values was found for some MSR 145 devices (see Fig. 2). Furthermore, the MSR 145 signal saturated at high irradiance values. For these reasons the MSR 145 devices were not used for the measurement network although their investment costs are very low.

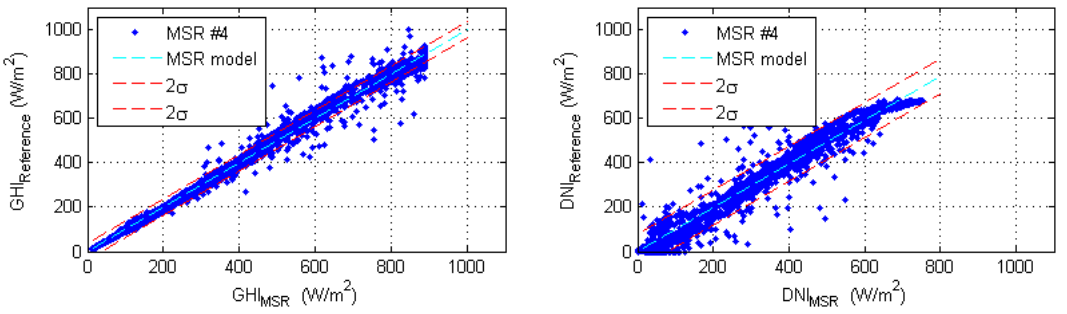

Fig. 1: Results of the MSR #4 with good agreement to reference

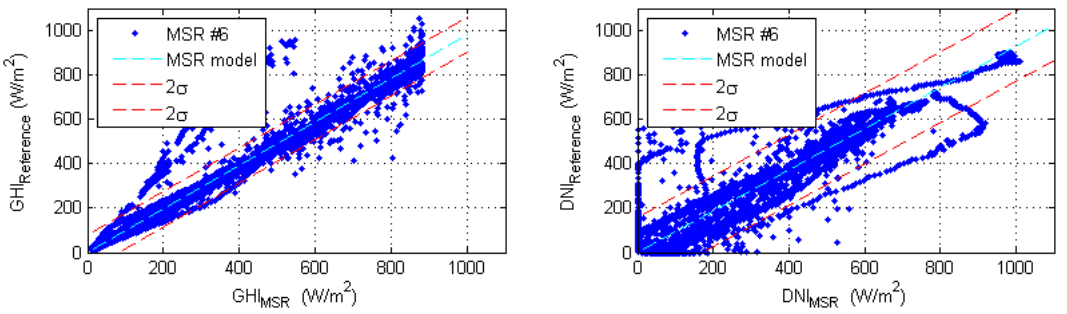

Fig. 2: Results of the MSR #6 with very poor agreement to reference

Figure 3 also shows the scatterplot for one of the three CS 300 pyranometers (CS #1). It consists of a dataset with 5589 measurements taken between August 7, 2012 and August 14, 2012. The measurements were taken each minute and only data was used when both SiP and reference did work properly and only during daytime. During the

measurement period clear-sky and overcast days occurred. Within the testing period technical problems with one SiP (Kipp&Zonen SP #1) occurred. Here only 387 measurements have been taken into account.

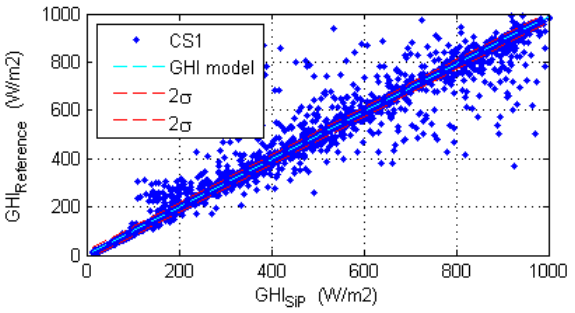

Fig. 3: Scatterplot of GHI measurements of SiP (CS #1) vs. PSA HP

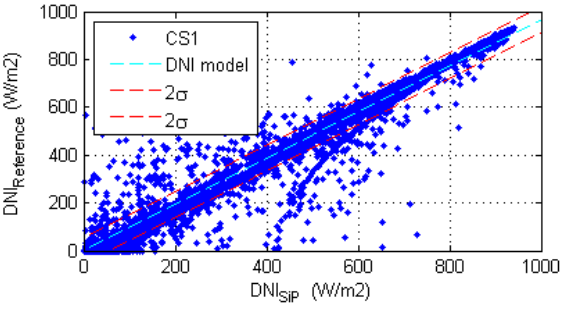

Fig. 4. Scatterplot of DNI measurements of SiP (CS #1) vs. PSA HP

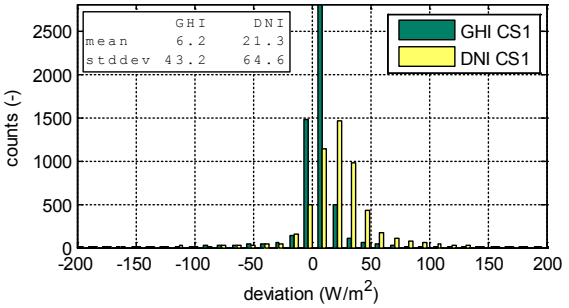

Fig. 5. Histogram of GHI and DNI deviations for CS #2

The regression graph in Fig. 3 and the confidence interval shows a good match between the reference and the measurements of the CS#1. The points that lie outside of the confidence intervals occurred mostly during overcast times. The reason is that the position of the reference meteo station is approx. 250 meters away from the SiP-Test field. This means during locally restricted changes (e.g. due to scattered cloud movement) the SiP and the PSA HP are showing different results.

As later shown in Equation (2) with knowledge of the DHI the GHI can be transformed to DNI values. The Transformation of the SiP values were done with the DHI value of the PSA HP station (Kipp&Zonen CMP21). Figure 2.3 shows the scatterplot of the pyrheliometer of the PSA HP (Reference) and the transformed DNI value of the SiP. Comparing Figures 3 and 4 it is observed that the deviation of GHI measurements occur more likely at higher values whereas the deviations of DNI occur more likely at lower values. This holds for all SiPs, see appendix. The reason is once again the local distance between PSA HP and SiPs. High DNI values correspond to a non-overcast situation. This means measuring DHI at a different location does not influence the quality of the model (Eq. (2)). Having lower irradiance due to clouds and measuring DHI and GHI at different positions may most likely lead to deviations. In Fig. 5 the histograms of the deviations are plotted for both GHI and DNI. Both distributions show a typical characteristic. The mean value of the GHI deviations is 6.2 W/m^2 and its standard deviation is 43.2 W/m^2. When calculating the DNI the additional model error due to different positions of GHI and DHI measurements add to the former values. Thus, we obtain mean deviation of 21.3 W/m^2 and a standard deviation of 64.6 W/m². Table 2.1 summarizes all deviations of the 9 tested SiPs. Since the purpose is to have DNI maps, the value of standard deviation of DNI deviation was the critical value to decide which SiP will be chosen. For the use in solar thermal

power plants applications differences within the nine SiPs do not appear to be significant. Therefore, it has been decided to use the most economical solution, the Campbell CS300 in order to build up the grid of SiP sensors.

Table 1: Mean and standard deviations of SiP sensors.
* only a basis of 387 measurements (instead of 5589) is used.

Sensor	GHI deviation		DNI deviation	
	mean (W/m²)	std. deviation (W/m²)	mean (W/m²)	std. deviation (W/m²)
CS #1	6.2	43.2	21.3	64.6
CS #2	9.1	41.4	21.3	60.8
CS #3	-10.4	47.1	-0.2	63.9
SP #1*	-1.5	44.1	10.6	70.4
SP #2	6.4	42.2	20.0	56.5
SP #3	4.4	41.7	16.0	56.9
LI #1	7.2	45.0	21.1	58.9
LI #2	7.4	44.5	17.8	57.6
LI #3	5.5	41.7	18.5	54.7

3. Measuring network and first results

The measurement network was built with 20 Si-pyranometers in total. These sensors are distributed around the DISS (DIrect Solar Steam) test facility (for more information on the DISS facility, see [8]) on the PSA in Spain. Figure 6 shows the sensors of the network in a coordinate system. The measurement network covers a surface of about 350 x 280 m. There are four “diamonds” with one sensor for each of the four cardinal directions and one sensor in the center. The sensors are described with a three-digit name: ”XYZ”. The first two digits indicate the position of the diamond and the last one the position inside the diamond. For example, NEW stands for the sensor in the west of the north-east diamond. A data acquisition system is installed for each diamond and linked via WiFi to the central data acquisition system. Currently, the GHI-grid consists of 3 sensors of the model Kipp & Zonen SP Lite, 3 sensors of the model Li-Cor LI200 SZ and 14 sensors of the model Campbell CS300, see Table 2. The Kipp & Zonen and Li-Cor sensor were used in a previous measurement campaign and were already available. The Campbell sensors were bought for the measurement network.

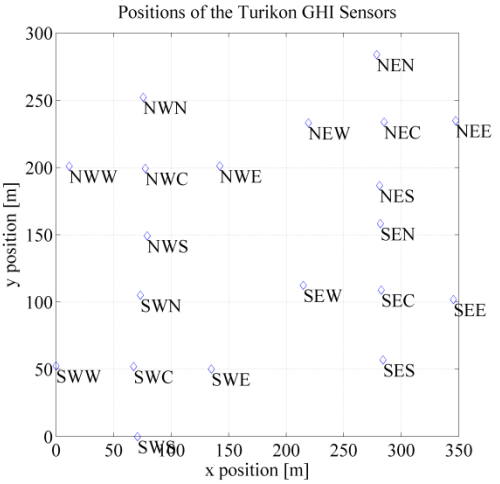

Fig. 6: Measurement network in a coordinate system

The data acquisition is carried out with four Campbell Scientific CR1000 data loggers, the Loggernet software and the visualization and data control software MDMS (Meteo Data Management System) from CSP Services and DLR, see [9].

Table 2: Different Si-pyranometer models in the measurement grid

Sensor	Model
SES,SEE, SEW	Kipp & Zonen SP-Lite 2
SEC, NES, NEW, NEC, NEE, NEN, NEW, NWN, NWC, NWW, NWS, SWN, SWE, SWC	Campbell CS300
SEN, SWW, SWS	Li-Cor LI200 SZ

Figure 7 shows the measured GHI between 12:13 and 12:19 on March 3, 2012. In the measured period there are two cloud fields moving over the GHI-grid. The curves clearly show the temporal effect of the individual position of each sensor in the grid, since each sensor is shaded at a different instant. It must be remarked, as well, that during the presented period, the GHI does not fall below 200 W/m². In fact, the DHI remains relatively constant or increases due to clouds. Furthermore, the diagram shows good agreement between the sensors between 12:15 and 12:16 when the network is not shaded.

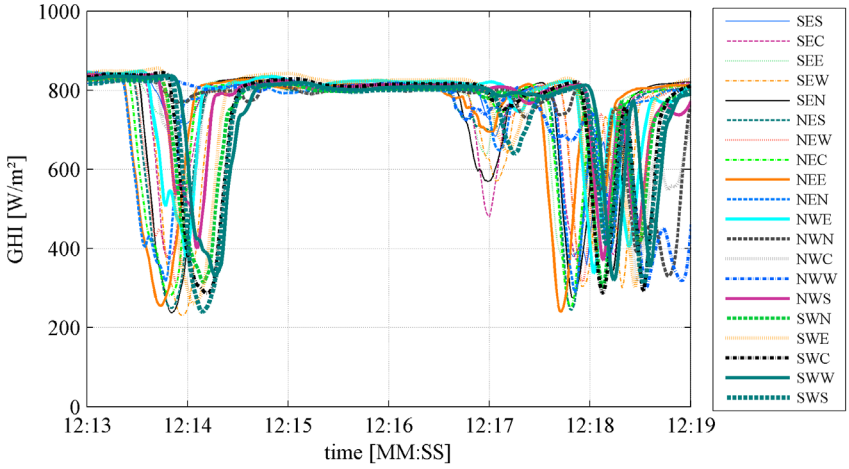

Fig. 7: Measured GHI curves for a cloud passing the GHI-grid on March 15, 2014.

4. Methodology to generate DNI maps

As already mentioned, the aim is to generate DNI-maps with a high temporal resolution from measurements of the irradiance network: A DNI map in this context is a set of DNI values representing the distribution of DNI across a certain area at a specific instant. The node points for DNI values can be arranged in structured, e.g. rectangular, or unstructured grid (e.g. triangles). The size of these DNI-maps should possibly overlap the dimensions of the measuring network. In fact, these maps shall serve as input for spatially distributed power plant models whose solar field is much bigger than the measurement network. In order to do so, two basic assumptions are made:

I. The diffuse irradiance within the measurement network can be approximated with the measured DHI from the closely located HP meteostation.
II. During days with a clearly-defined cloud direction and speed, their shape does not change significantly while moving over the measurement network.

By means of both assumptions, the DNI inside the boundaries of the network can be calculated first. Having determined a cloud movement vector from pictures taken from the shadow camera, in a second step, the DNI can be projected in cloud movement direction. In the following, this method is described in detail.

4.1. Determination of the DNI in the measuring network

The GHI is related to DNI and DHI via Eqn.1 where α represents the solar altitude angle.

$$GHI = DNI \cdot \sin \alpha + DHI \tag{1}$$

Several meteorological stations with pyrheliometers and shaded pyranometers are available at PSA close to the GHI-grid, that provide measurements of diffuse, direct, and global irradiance in a temporal resolution of 10 s, see example in Fig. 8. In the sample data set clouds mainly occur between 12:00 and 15:00. These clouds represent disturbances on the measured DNI which are limited to the shadow area of the clouds. In our example, the opacity of the clouds is high leading to a drop of DNI down to almost zero. Although the DNI is reduced under the clouds the values of DHI rise from below 200 W/m² up to 300 W/m² during the cloudy period. This increase is visible already a few minutes before the clouds arrive (right before 12:00) and remains during the cloudy period. The increase in diffuse irradiance originates from irradiance scattered by the clouds and also reflections from the cloud. While the impact on DNI is restricted to the shaded area the impact of clouds on diffuse irradiance is noticeable in areas with high DNI.

Therefore, assumption (I) from the previous section appears to be applicable. As long as the DHI is measured close to the irradiance measuring network, the DNI at each sensor can be calculated from the measured GHI. Using Eq. 1 the DNI for each sensor i can be calculated from the measured global irradiance (at each sensor) and diffuse irradiance measured at the HP meteo station with shaded thermopile pyranometers (index HP).

$$DNI_i = (GHI - DHI_{\mathrm{HP}}) / \sin \alpha \tag{2}$$

Figure 9 shows the calculated DNI at each sensor of the measurement grid for the same time period as in Fig. 7. In contrast to the GHI in Fig. 3 the DNI in Fig. 5 approaches to almost zero when clouds pass by. During the period where the sensors are not shaded (between 12:15 and 12:16) the DNI coincidentally approximately equals the value of the GHI. This coincidence can be confirmed by examining the curves for GHI and DNI in Fig. 4 around noon.

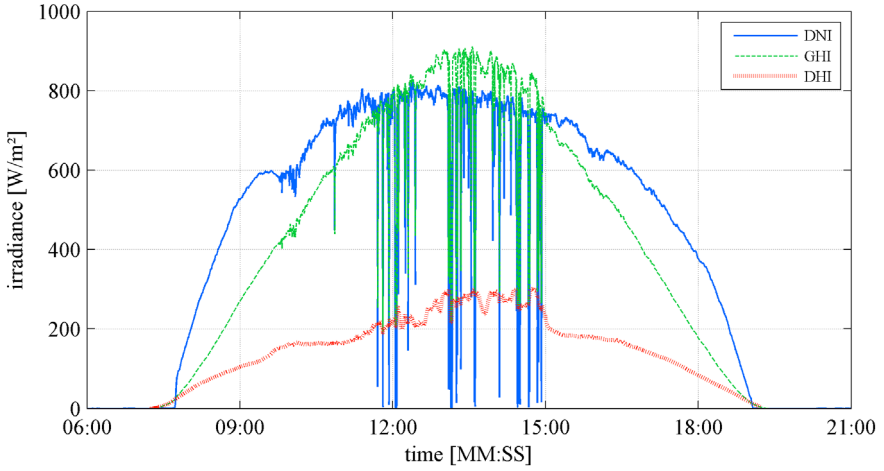

Fig. 8: DNI, GHI, and DHI from one of the meteo-stations with solar tracker and thermal sensors at the PSA for March 15, 2014

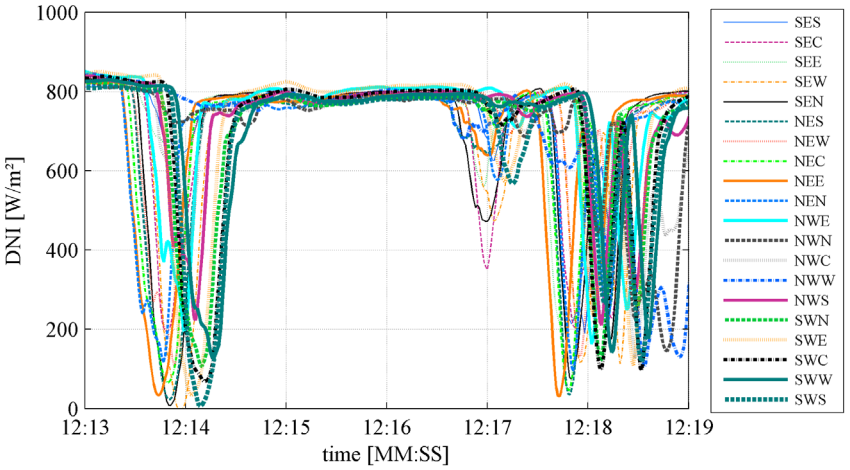

Fig. 9: Calculated DNI for the same period as in Fig. 3

4.2. Procedure for the creation of a DNI-map in cloud direction

In the following, the process of creating a DNI-map is shown. Starting point is the area covered by the measurement network and represented by 20 single DNI data points. Values between the nodes can be interpolated. In that way a time series of "core" DNI maps is given by the measured values at each instant. This "core" map, which covers all points with position x and y for the instant t is denoted M in Eq. 3:

$$M(x,y,t) = f(DNI_i(t)) \tag{3}$$

By using assumption (II), according to which the cloud shape does not change in the near surrounding of the measurement network, the DNI pattern obtained in the measurement area can be extrapolated in the direction of cloud movement. This allows to artificially enlarging the extension of the area covered by DNI values. The result is an extended map, denoted M_{ext} in Eq. 4:

$$M_{ext}(x,y,t) = f(DNI_i(t), DNI_i(t\text{-}k*\Delta t)) \quad \text{with } k = 1\ldots n \tag{4}$$

where Δt describes the time step and n the number of considered time steps backwards in M_{ext} at the time instant t. This extended map at t is thus composed of the DNI at this instant and the values measured at instants in the near past. The location of these past values is obtained from the cloud movement vector.

Figure 10 shows the above-described process in six steps (a to f) for the time instant t at 12:14:00 on March 15, 2014. All diagrams show the DNI-map in a coordinate system. In (a) the data points of the measurement network are shown. Grey lines show the so-called Delaunay-Triangulation, a common method to determine the triangle in which interpolation is possible with the given database. The bold line shows the envelope of the data grid, which defines the spatial limit for the interpolation. In (b) the core map M (compare with Eq. 3) is visualized in a contour-plot obtained from linear interpolation. As shown, there is a cloud that partially covers the measurement network. In the center of the cloud's shadow, the DNI is almost zero. Considering the basic assumption II, the cloud movement vector is known and the cloud shape is considered to remain unchanged within the examined period. If so, as shown in (c), the irradiance at the data point i, $DNI_i(t)$, is known and value at the same point, measured a time-step before $DNI_i(t\text{-}\Delta t)$ was transposed with the cloud vector. In the example Δt = 3s. Since the envelope (black bold line) contains the newest measured DNI values at the timepoint t, transposed values inside the envelope from the timepoint (t-Δt) are discarded. Diagram (d) shows the Delaunay-Triangulation of the enlarged area, combining information of data points from of t and (t-Δt). By continuing this process, the data grid is systematically enlarged.

Diagram (e) shows the data grid which contains data points from the time instant t back to (t-90 s). In (f) a contour plot of the extended DNI-map M_{ext} (compare with Eq. 4) is shown. In comparison with (b) the DNI-map is enlarged by the colored area outside the bold envelope.

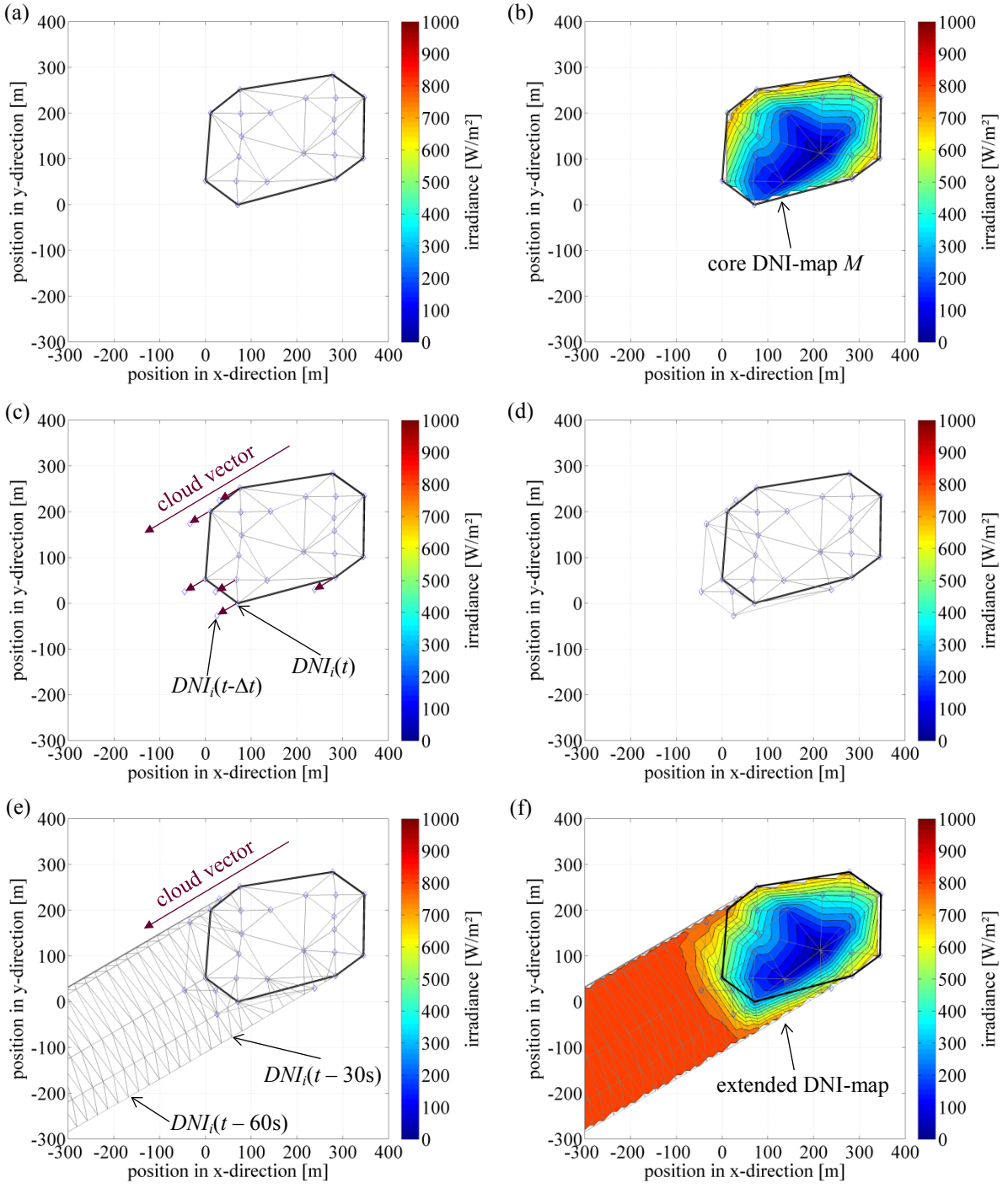

Fig. 10: Creation of a DNI-Map for time instant 12:14:00 on March 15 2014. The color bars represent the DNI in W/m².

It must be noted, that no information in the blank areas (diagrams, Fig. 10) is available. The extended DNI-map will have the shape of a tube whose length and width depend on the direction and speed of the cloud vector.

5. DNI-Maps: Application of the method

In order to apply the methodology, the speed and direction of the cloud movement must be determined. Fig. 11 shows two pictures of the terrain of the PSA on March 15 2014, where the right picture is taken 30 s after the picture on the left. The pictures show the DISS test-facility which is north-south oriented and the shadow of a cloud front moving over the PSA roughly in north-east direction (from where the cloud comes from). By orthogonalizing these pictures the direction and velocity were manually determined for various time-points during this cloudy period.

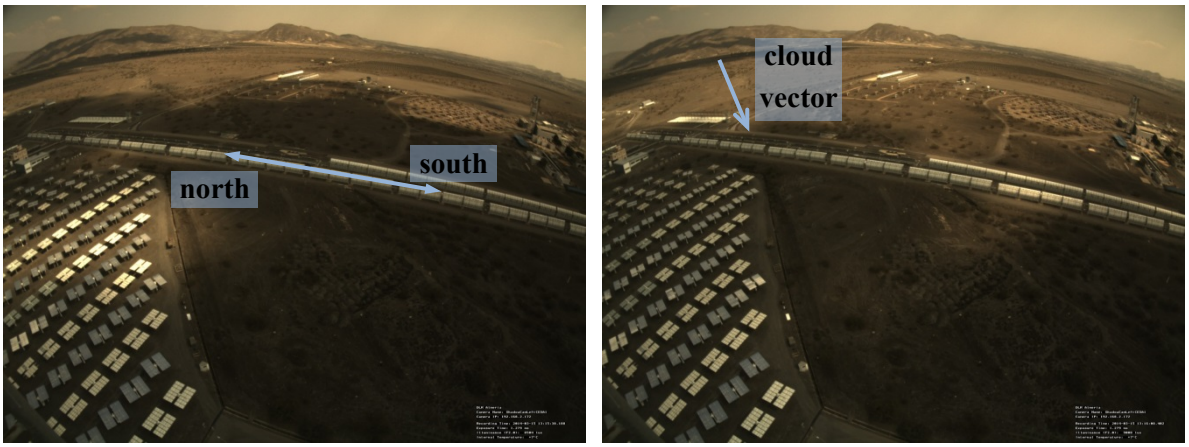

Fig. 11: Pictures in 30s time lag of cloud movement from north-east over the PSA on March 15 2014

Figure 12 shows a sequence of DNI-maps that have been created with the presented methodology for a period of 45 s from 12:05:57 to 12:06:42. In this period, clouds move over the measurement network with a velocity of 7.6 m/s and with an angle of 66° (counted from north) as shown in the upper left diagram. In the same diagram, the shadow of a cloud appears at the east extremity of the measurement network. In the following diagrams this cloud is visible, as well, and moves through the measurement network. From 12:06:24 on the cloud begins to overlap the black envelope whereas in the last one the cloud is completely outside the envelope.

The movement of the cloud outside the envelope is extrapolated with the presented methodology assuming an unchanged cloud shape. Although the methodology has not been validated, yet, two aspects indicate its applicability:

- The shape of the shadow of the cloud remains more or less constant while passing over the network. Slight deviations of the shape can either be explained by a slightly changing shape or due to the limited number of data points in the network (20 sensors).
- The cloud appears to move over the network in the same direction as derived from pictures of the shadow camera.

Both statements confirm assumption (II) of section 4.1 at least for the examined period that is presented here. Nevertheless, a more systematic validation of the methodology shall follow in near future.

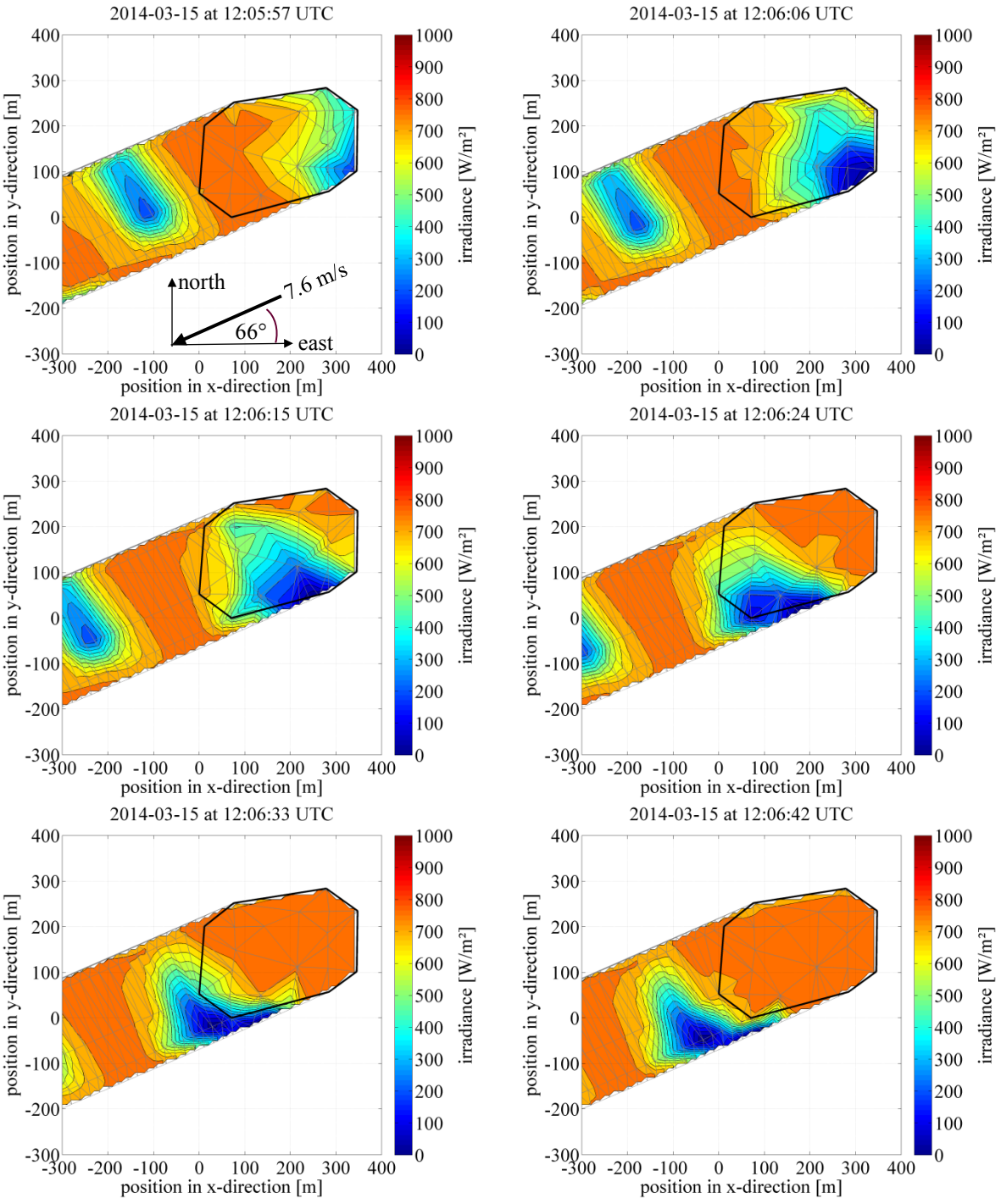

Fig. 12: Sequence of 6 DNI Maps on March 3 2014 between 12:05:57 and 12:06:42. The color bars represent the DNI in W/m².

Conclusion

The motivation and aim to build a spatially-distributed irradiance measurement network was outlined. Various sensors were tested. The most cost-effective solution would have been the illuminance meter MSR 145 of the Swiss company MSR. However, since the measurement quality of these devices varied, the measurement network was finally built with silicon pyranometers at the PSA in Spain. This network is in operation since 2013 and the measured GHI signals show the effect of the different position of each sensor during the passage of cloud fields. A methodology has been presented that allows generating time-series of DNI-maps. In a first step, the value for the DNI has been approximated at each sensor in the network using the measured DHI value of a nearby shaded thermal pyranometers at PSA. Furthermore, orthogonalized pictures from a shadow camera have been used to determine a cloud movement vector. Under the assumption that the cloud shape does not significantly change for a certain period and that the cloud movement vector is correctly determined, DNI values inside the measurement network can be shifted in the direction of the cloud vector. In that manner, DNI-maps have been created that overlap the measurement network. An exemplary time-series of a cloud passage has been presented. This time-series underlines the applicability of the methodology.

Acknowledgements

The authors would like to thank the German Federal State of North Rhine-Westphalia and the European Regional Development Fund for the financial support of the project TURIKON in the frame of the program progress. NRW and the goal 2-program 2007-2013, Phase VI (Grant No. 64.65.69-EN-2019).

The authors also would like to thank the CIEMAT (Centro de Investigaciones Energéticas, Medioambientales y Tecnológicas) for hosting the activities of the Turikon project on the PSA (Plataforma Solar de Almería).

6. References

[1] Giostri, A., 2014, "Transient effects in linear concentrating solar thermal power plants," Ph.D. thesis, Politecnico di Milano, Milan.
[2] Wittmann, M., Hirsch, T., and Eck, M., 2009, "Some Aspects on Parabolic Trough Field Operation with Oil as a Heat Transfer Fluid," 15th SolarPACES Symposium, Berlin, pp. 9.
[3] Eck, M., and Hirsch, T., 2007, "Dynamics and control of parabolic trough collector loops with direct steam generation," Solar Energy, 81 (2), pp. 268-279.
[4] Yang, H., Kurtz, B., Nguyen, D., et al., 2014, "Solar irradiance forecasting using a ground-based sky imager developed at UC San Diego," Solar Energy, 103 (0), pp. 502-524.
[5] Afshin, A., Oahu solar measurement grid, April 2014, http://www.nrel.gov/midc/oahu_archive/.
[6] Chow, C. W., Urquhart, B., Lave, M., et al., 2011, "Intra-hour forecasting with a total sky imager at the UC San Diego solar energy testbed," Solar Energy, 85, pp. 2881-2893.
[7] Bosch, J. L., and Kleissl, J., 2013, "Cloud motion vectors from a network of ground sensors in a solar power plant," Solar Energy, 95, pp. 13-20.
[8] Bosch, J. L., Zheng, Y., and Kleissl, J., 2013, "Deriving cloud velocity from an array of solar radiation measurements," Solar Energy, 87, pp. 196-203.
[9] Geuder, Wolfertstetter F., Wilbert S., Schueler D., Affolter R., Luepfert E., Espinar, B. Screening and flagging of solar irradiation and ancillary meteorological data. 20th SolarPACES conference 2014, Bejing, China.